Ice front blocking of ocean heat transport to an Antarctic ice shelf

Anna K. Wåhlin, Nadine Steiger, Elin Darelius-Chiche, Karen M. Assmann, Mirjam S. Glessmer, Ho Kyung Ha, Laura Herraiz-Borreguero, Céline Heuzé, Adrian Jenkins, Tae-Wan Kim, et al.

Ice front blocking of ocean heat transport to an Antarctic ice shelf

Wåhlin, A.K*., Steiger, N., Darelius, E., Assmann, K.M., Glessmer, M.S., Ha, H.K., Herraiz-Borreguero, L., Heuzé, C., Jenkins, A., Kim, T.W., Mazur, A.K., Sommeria, J., Viboud, S.

Correspondence to: awahlin@gu.se

Introductory paragraph:

Mass loss from the Antarctic Ice Sheet to the ocean has increased in recent decades, largely because the thinning of its floating ice shelves has allowed the outflow of grounded ice to accelerate[1,2]. Enhanced basal melting of the ice shelves is thought to be the ultimate driver of change[2,3], motivating a recent focus on the processes that control ocean heat transport onto and across the seabed of the Antarctic continental shelf towards the ice[4–6]. However, the shoreward heat flux typically far exceeds that required to match observed melt rates[2,7,8], suggesting other critical controls. Here we show that the depth-independent (barotropic) component of the flow towards an ice shelf is blocked by the dramatic step shape of the ice front, and that only the depth-varying (baroclinic) component, typically much smaller, can enter the sub-ice cavity. Our results arise from direct observations of the Getz Ice Shelf system and laboratory experiments on a rotating platform. A similar blocking of the barotropic component may occur in other areas with comparable ice-bathymetry configurations, which may explain why changes in the density structure of the water column have been found to be a better indicator of basal melt rate variability than the heat transported onto the continental shelf[9]. Representing the step topography of the ice front accurately in models is thus important for simulating the ocean heat fluxes and induced melt rates.

Main text:

The fate of the Antarctic Ice Sheet is the greatest remaining uncertainty when predicting future sea level[10]. Estimates of its contribution to global sea-level rise range from none to a catastrophic > 5 cm/year[10–12] (4 m by the year 2100). The ice sheet drains into the ocean where it terminates in floating ice shelves, overlying vast sub-ice cavities. These buttress the flow of the ice sheet, regulating the speed at which it flows into the ocean[13]. Rapid thinning of ice shelves in coastal regions with warm ocean water on the continental shelf is accelerating the outflow from the ice sheet[1,2]. The perceived reason - although rarely observed directly[14] - is that ocean currents deliver more warm water to the ice shelf cavities, causing increased basal melt. These currents originate in a reservoir of warm and salty water, known as Circumpolar Deep Water (CDW)[15], residing at 300-1000 m depth in the Southern Ocean. Substantial amounts of dense CDW are carried onto the continental shelf by various mechanisms[4–7,16], but only a fraction of this is needed to explain observed basal melt rates[17]. The CDW flows southward in deep troughs that crosscut the continental shelf[4,18–21]. The currents are steered by the bathymetry and move with shallower water to the left of the flow direction[22–24] so southward transport occurs along the eastern, and northward on western, flanks of the troughs[19,25]. The flow is a combination of barotropic (vertically constant, wind-driven[26,27]) and baroclinic (vertically varying, density-driven) currents. Although the barotropic velocities often dominate[27,28], most of the heat is contained in the warm dense water below the thermocline where the baroclinic component typically enhances the flow.

In order to enter the ice shelf cavity the currents must pass the ice front - a wall of ice protruding from the surface to depths of 250 – 500 m. This front imposes an abrupt change in the thickness of the water column, potentially disrupting the topographically steered flow towards it[29]. Logistical challenges generally prevent observations near the ice front, and estimates of oceanic heat transport towards the ice shelves are based on moorings placed at a 'safe' distance (at least a few km) away from the ice front.

To examine the effect of the ice front on the along-trough current, three moorings equipped with velocity profilers and loggers for temperature, salinity, and pressure were placed in a deep trough leading to Getz Ice Shelf (Fig. 1). Two of the moorings were positioned 14 km and 11 km away from the ice front at depths of 600 and 700 m respectively, while the third was placed 700-800 m from the front at 600 m depth. The ice front draft is 250-300 m[30], and its position was constant during the two years of measurements (Fig. 1).

Feather-plots of the average velocity at various depths for the three moorings (Fig. 1, Methods, full time series in Extended Data Figs 1-3) show a persistent current up to 30 cm/s directed towards the ice shelf, parallel to the local bathymetry[8]. The velocity at the near-front mooring was less than one third of those in the channel and deflected westward by up to 45°.

Separating the currents into barotropic and baroclinic components (Fig. 2, Methods, Extended Data Figs 4-5) reveals that while GW1 and GW2 had significant barotropic along-slope flow (7.5 and 10 cm/s) with a baroclinic amplification in the warm bottom layer, the velocity at GW3 had a comparatively small barotropic component (0.1 cm/s) and was dominated by the baroclinic flow in the warm bottom layer. The direction of the baroclinic flow at GW3 is into the ice shelf cavity, i.e. parallel to the local topography and orthogonal to the ice front. It should be noted however that the bathymetry underneath the ice shelf has not yet been surveyed[31]. In the un-surveyed areas south of mooring GW3 the compilation used in Fig. 1 is based on gravity inversions associated with high uncertainty[31]. If there are underwater features such as submarine ridges and seamounts present underneath the ice shelf these might redirect the flow.

The strong correlation between the velocity at GW3 and the baroclinic velocities at GW1 and GW2 (Fig. 2 and Table 1, dark blue fields), indicates that the baroclinic current component at GW1 and GW2 is continuing to GW3. The barotropic component however has no significant correlation to the GW3 velocity, suggesting that it is diverted along the ice shelf front before it reaches GW3 (Fig. 1, Fig. 2). This is further evidenced by the high correlation between bottom temperature/density anomalies at GW2 and GW3 (both at the 600 m isobaths, Table 1, dark blue field). The barotropic component of the flow carries about 70% of the total heat transport (Extended Data Table 1, Extended Data Figure 6, Methods) at GW1 and GW2, similar to values on the central Amundsen Shelf[27], while at GW3 it carries only 3-10% (based on the more realistic methods (i) or (ii) for estimating barotropic velocity, see Methods). The heat transport is dominated by the mean flow rather than the fluctuations assessed in Table 1 (Extended Data Table 1).

The observed behavior of the velocity components at the ice front can be explained by geostrophic ocean dynamics[22,29]. Geostrophic currents are non-divergent and therefore flow parallel to lines of constant water column thickness, or, in the open ocean, lines of constant depth[22,24]. This is the reason why the currents in the deep troughs are so strongly steered by the (comparatively gentle) topography. However, where a floating ice shelf with a considerable draft overlies the ocean, the water column thickness is no longer equal to the depth. Applied to the present setting this means that barotropic currents approaching the ice front along depth contours will be diverted due to the change in water column thickness (Methods) and may be blocked entirely without reaching the ice shelf cavity[29]. Baroclinic flow, on the other hand, can move along depth contours into the ice shelf cavity, provided the thermocline is deeper than the ice shelf draft.

In order to explore this phenomenon in a controlled environment, experiments were conducted in the 13-m diameter rotating Coriolis platform in Grenoble, France. A simplified bathymetry - a v-shaped trough - was placed in a 90-cm deep tank filled with fresh water (Fig. 3). A source was placed on the right flank (facing North) of the trough, pumping fresh water to set up a barotropic current, or saline (denser) water for a baroclinic bottom current. At the far end of the trough a plexiglass ice shelf with adjustable draft was placed. A detailed description of the experimental setup is presented in Methods.

The experimental results agree qualitatively with the geostrophic dynamics outlined above. The current followed the trough flank towards the ice shelf, and away from it on the opposite side, in similarity with observations[19,25] (Fig. 4). Placing an ice shelf with near-zero draft on top of the trough (Fig. 4A) had no visible impact on the circulation. However, a sloping ice shelf with zero draft at the front and 30 cm at the back (Fig. 4B) caused the barotropic flow to change direction and follow lines of constant water thickness into the ice shelf cavity. A horizontal ice shelf with 30 cm draft (Fig. 4C) blocked the current from entering the cavity.

The baroclinic currents (Extended Data Fig. 9) continued mostly unaffected into the ice shelf cavity for all ice shelf drafts and shapes.

The observational and experimental results presented here enhance our understanding of how changes in oceanic heat transport on the continental shelf can impact basal melt. Barotropic flow is blocked, either partially or entirely, depending on the ice front geometry, from entering the cavity. Changes in the water temperature and/or baroclinic flow, on the other hand, will change the amount of heat that flows into the cavity. How much of it is ultimately used for basal melting depends on the cavity efficiency[32]. The results explain why changes in the thickness of the warm water layer seem to be a more reliable indicator of melt rate variability than e.g. ocean transports across the shelf break. Changes in the vertical structure of the water column is a better diagnostic of the critical baroclinic heat transport.

Since flows toward ice shelf cavities nearly always have a substantial barotropic component[8,26,27,33], the findings have broad implications for calculations of ocean heat transport to ice shelf cavities. For example, the measured heat transport along the Siple Trough is 2.27-2.8 TW (Extended Data Table 1) - sufficient to melt about 250-300 Gt/yr ice and twice the total basal melt, 136 Gt/yr, that the entire Getz ice shelf experiences[17]. However, due to the abrupt front shape only one sixth (0.47 TW) of the heat that flows past GW1-2 enters the cavity. The results indicate that the floating ice shelves not only give back-stress, mechanically slowing down the inland ice sheet[13], but that they also protect the vulnerable grounded ice by blocking a large portion of the warm ocean currents from reaching the cavity. The thickness and shape of the ice front may provide a critical and evolving control that needs to be incorporated accurately in models: Were an ice front to thin substantially, or to retreat back (or advance) to a region with larger underwater features steering the warm currents towards the cavity, then the heat flux to the ice sheet could change dramatically. Rare observations from inside the cavity[14,34] are needed to determine e.g. how much of the heat transport that eventually reaches the vulnerable grounding zones.

References:

1. Shepherd, A., Fricker, H. A. & Farrell, S. L. Trends and connections across the Antarctic cryosphere. *Nature* **558**, 223–232 (2018).

2. Pritchard, H. D. *et al.* Antarctic ice-sheet loss driven by basal melting of ice shelves. *Nature* **484**, 502–505 (2012).

3. Liu, Y. *et al.* Ocean-driven thinning enhances iceberg calving and retreat of Antarctic

ice shelves. *Proc. Natl. Acad. Sci. U. S. A.* **112**, 3263–8 (2015).

4. Thoma, M., Jenkins, A., Holland, D. & Jacobs, S. Modelling Circumpolar Deep Water intrusions on the Amundsen Sea continental shelf , Antarctica. *Geophys. Res. Lett.* **35**, 1–6 (2008).

5. Wåhlin, A. K. *et al.* Some Implications of Ekman Layer Dynamics for Cross-Shelf Exchange in the Amundsen Sea. *J. Phys. Oceanogr.* **42**, 1461–1474 (2012).

6. Darelius, E., Fer, I. & Nicholls, K. W. Observed vulnerability of Filchner-Ronne Ice Shelf to wind-driven inflow of warm deep water. *Nat. Commun.* **7:12300**, (2016).

7. Palóczy, A., Gille, S. T. & Mcclean, J. L. Oceanic Heat Delivery to the Antarctic Continental Shelf : Large-Scale , Low-Frequency Variability. *J. Geophys. Res.* **123**, 7678–7701 (2018).

8. Assmann, K. M., Darelius, E., Wåhlin, A. K., Kim, T. W. & Lee, S. H. Warm Circumpolar Deep Water at the western Getz Ice Shelf Front, Antarctica. *Geophys. Res. Lett.* **46**, 870–878 (2019).

9. Jenkins, A. *et al.* West Antarctic Ice Sheet retreat in the Amundsen Sea driven by decadal oceanic variability. *Nat. Geosci.* (2018). doi:10.1038/s41561-018-0207-4

10. IPCC. *Climate Change 2014: Synthesis Report. Contribution of Working Groups I, II and III to the Fifth Assessment Report of the Intergovernmental Panel on Climate Change*. (IPCC, 2014).

11. IMBIEteam. Mass balance of the Antarctic ice sheet from 1992 to 2017. *Nature* **558**, 219–222 (2018).

12. DeConto, R. M. & Pollard, D. Contribution of Antarctica to past and future sea-level rise. *Nature* **531**, 591–597 (2016).

13. Scambos, T. A., Bohlander, J. A., Shuman, C. A. & Skvarca, P. Glacier acceleration and thinning after ice shelf collapse in the Larsen B embayment, Antarctica. *Geophys. Res. Lett.* **31**, 2001–2004 (2004).

14. Jenkins, A. *et al.* Observations beneath Pine Island Glacier in West-Antarctica and implications for its retreat. *Nat. Geosci.* **3**, 468–472 (2010).

15. Callahan, J. E. The structure and circulation of Deep Water in the Antarctic. *Deep Sea*

Res. **19**, 563–575 (1972).

16. Thompson, A. F., Stewart, A. L., Spence, P. & Heywood, K. J. The Antarctic Slope Current in a Changing Climate. *Rev. Geophys.* **56**, 741–770 (2018).

17. Depoorter, M. A. *et al.* Calving fluxes and basal melt rates of Antarctic ice shelves. *Nature* **502**, 89–92 (2013).

18. Wåhlin, A. K., Yuan, X., Björk, G. & Nohr, C. Inflow of Warm Circumpolar Deep Water in the Central Amundsen Shelf*. *J. Phys. Oceanogr.* **40**, 1427–1434 (2010).

19. Herraiz-Borreguero, L. *et al.* Circulation of modified Circumpolar Deep Water and basal melt beneath the Amery Ice Shelf, East Antarctica. *J. Geophys. Res. Ocean.* **120**, 3098–3112 (2015).

20. Nakayama, Y., Menemenlis, D., Zhang, H., Schodlok, M. & Rignot, E. Origin of Circumpolar Deep Water intruding onto the Amundsen and Bellingshausen Sea continental shelves. *Nat. Commun.* **9**, 1–9 (2014).

21. St-Laurent, P., Klinck, J. M., Dinniman, M. S. & Oceanography, C. P. On the Role of Coastal Troughs in the Circulation of Warm Circumpolar Deep Water on Antarctic Shelves. *J. Phys. Oceanogr.* **43**, 51–64 (2013).

22. Cushman-Roisin, B. & Beckers, J.-M. *Introduction to Geophyscial Fluid Dynamics: Physical and numerical aspects*. (Prentics-Hall Inc., 2011).

23. Nof, D. The translation of isolated cold eddies on a sloping bottom. *Deep. Res. Part A-Oceanographic Res. Pap.* **30**, 171–182 (1983).

24. Wåhlin, A. K. Topographic advection of dense bottom water. *J. Fluid Mech.* **510**, 95–104 (2004).

25. Ha, H. K. *et al.* Circulation and Modification of Warm Deep Water on the Central Amundsen Shelf. *J. Phys. Oceanogr.* **44**, 1493–1501 (2014).

26. Wåhlin, A. K. *et al.* Variability of Warm Deep Water Inflow in a Submarine Trough on the Amundsen Sea Shelf. *J. Phys. Oceanogr.* **43**, 2054–2070 (2013).

27. Kalén, O. *et al.* Is the oceanic heat flux on the central Amundsen sea shelf caused by barotropic or baroclinic currents? *Deep. Res. Part II Top. Stud. Oceanogr.* (2016). doi:10.1016/j.dsr2.2015.07.014

28. Rignot, E., Jacobs, S., Mouginot, J. & Scheuchl, B. Ice-Shelf Melting Around Antarctica. *Science (80-.).* **341**, 266–270 (2013).

29. Grosfeld, K., Gerdes, R. & Determann, J. Thermohaline circulation and interaction between ice shelf cavities and the adjacent open ocean. *J. Geophys. Res. Ocean.* **102**, 15595–15610 (1997).

30. Jacobs, S. *et al.* Getz Ice Shelf Melting Response to Changes in Ocean Forcing. *J. Geophys. Res. - Ocean.* **118**, 4152–4168 (2013).

31. Arndt, J. E. *et al.* The International Bathymetric Chart of the Southern Ocean (IBCSO) Version 1.0 - A new bathymetric compilation covering circum-Antarctic waters. *Geophys. Res. Lett.* **40**, 311–3117 (2013).

32. Little, C. M., Gnanadesikan, A. & Oppenheimer, M. How ice shelf morphology controls basal melting. *J. Geophys. Res.* **114**, C12007 (2009).

33. Miles, T. *et al.* Glider observations of the Dotson Ice Shelf outflow. *Deep Sea Res. Part II Top. Stud. Oceanogr.* **123**, 16–29 (2015).

34. Nicholls, K. W. *et al.* Measurements beneath an Antarctic ice shelf using an autonomous underwater vehicle. **33**, 2–5 (2006).

35. Gade, H. Melting of ice in sea water: A primitive model with application to the Antarctic ice shelf and icebergs. *J. Phys. Oceanogr.* **9**, 189–198 (1979).

Acknowledgments:

The experiments were supported by the European Community's H2020 through the grant to HYDRALAB-PLUS, Contract no. 654110. We gratefully acknowledge grant support for the authors as follows: ED and NS, Norwegian Research Council through grant no. 267660 (TOBACO) and 231549 (WARM); AJ from the UK Natural Environment Research Council through grant no. NE/L013770/1 (FISS), AW from the Swedish Research Council and the Swedish Foundation for Strategic Research through the Swedish Maritime Robotics Center (SMaRC), TWK from the Korea Polar Research Institute grant KOPRI PE19060. Thanks to I. Fer for lending instrumentation to GW1 and GW2.

Author contributions:

AKW proposed the research. AKW, NS, ED and KA wrote the first draft. JS assisted with analyses and repository of laboratory data. All authors contributed to the laboratory experiments, to data processing, and/or to the field work. AKW, NS, SV, AKM prepared the figures. All authors read and commented on the text.

Author information:

Corresponding author: Dr. A.K. Wåhlin, email: awahlin@gu.se

No authors have any competing interests.

Author affiliations:

Wåhlin, A. K: Department of Marine Sciences, University of Gothenburg, Sweden

Steiger, N.: Bjerknes Centre for Climate Research and Geophysical Institute, University of Bergen, Norway

Darelius, E.: Geophysical Institute, University of Bergen, Norway

Assmann, K.M.: Department of Marine Sciences, University of Gothenburg, Sweden

Glessmer, M.S.: Leibniz Institute of Science and Mathematics Education, Kiel, Germany

Ha, H.K., Inha University, South Korea

Herraiz-Borreguero, L., Commonwealth Scientific and Industrial Research Organisation (CSIRO), Hobart, Australia

Heuzé, C.: Department of Earth Sciences, University of Gothenburg, Sweden

Jenkins, A., British Antarctic Survey, Cambridge, United Kongdom

Kim, T.W., Korea Polar Research Institute, South Korea

Mazur, A.K: Department of Marine Sciences, University of Gothenburg, Sweden

Sommeria, J., Laboratoire des Ecoulements Geophysiques et Industriels Domaine Universitaire, Grenoble, France

Viboud, S.: Laboratoire des Ecoulements Geophysiques et Industriels Domaine Universitaire, Grenoble, France

Table 1. Correlation between Getz moorings

	ρ_B GW1	**T_B GW2**	**ρ_B GW3**	**U GW3**
T_B GW2	**0.62 (0.55)**	-	-	-
ρ_B GW3	**0.67 (0.58)**	**0.92 (0.83)**	-	-
U_{BC} GW1	**0.54 (0.46)**	**0.71 (0.62)**	**0.77 (0.67)**	**0.66 (0.53)**
U_{BT} GW1	-0.09 (-0.03)	-0.08 (0.05)	-0.25 (-0.1)	-0.08 (0.02)
U_{BC} GW2	**0.43 (0.36)**	**0.54 (0.49)**	**0.53 (0.45)**	**0.67 (0.51)**
U_{BT} GW2	0.15 (0.03)	0.20 (0.01)	0.09 (0.1)	0.23 (0.23)
U GW3	**0.51 (0.36)**	**0.5 (0.39)**	**0.65 (0.57)**	-

Correlation coefficients between combinations of bottom density ρ_B (or bottom temperature T_B for GW2, which had a broken conductivity sensor and hence no bottom density) and along-slope bottom velocity U, as well as the barotropic (U_{BT}) and baroclinic (U_{BC}) components of bottom velocity for the three moorings GW1, GW2 and GW3. Numbers shown are correlations between the indicated quantities based on 10-day average values and, within parentheses, 3-day averages. Bold numbers indicate that the correlations are significant at the 99.99% level. Dark blue fields indicate the key correlations discussed in the text.

Captions:

Figure 1. Blocking of topographically steered current at the Getz Ice Shelf front. (a) Mooring locations and time averaged velocities from three moorings (GW1-3) are shown as feather plots on top of the local bathymetry[31]. Velocities are color coded with conservative temperature θ and depth-averaged in 50 m bins starting at the bottom. The lowermost (red, warmest) and uppermost (blue, coldest) bin depths are quoted near the corresponding arrow. Also shown is the location of the ice front in January 2016, 2017 and 2018 (blue lines, Methods). Lower panels show conservative temperature θ versus absolute salinity S_A for (b) GW1 (c) GW2 (d) GW3 in green hues, gray dots are the data from all moorings. Red squares indicate Circumpolar Deep Water temperature- and salinity range[15], blue thick line is the mixing line between CDW and glacier meltwater[35], lower black thin line is the freezing point (T_f). The lack of data points near salinity 34.5 g kg^{-1} in GW2 is due to the fact that GW2 only had two salinity sensors (Extended Data Figure 2), of which one was faulty for a period of time (see Methods). Mooring temperature- and velocity time series are shown in Extended Data Figs. 1 - 3.

Figure 2: **Baroclinic velocity component at GW2 is similar to total velocity at GW3.** Three-day average along-slope velocity (color bar, m/s), with isotherms (black contours, every 0.5 degrees, thick black line shows the 0 degree isotherm) (a) Total alongslope velocity at GW2 (b) Baroclinic velocity component (Methods) at GW2 (c) Total alongslope velocity at GW3. Note that the topmost sensor on GW2 was at 357 m depth while at GW3 it was at 288 m depth (Extended Data Figure 2, Extended Data Figure 3).

Figure 3. Experimental set-up and difference between barotropic and baroclinic flow. (a) Sketch of the experiment. Side view sketches of the ice shelf (light gray), bottom (dark gray) and water (blue) with ice shelf draft 0 cm (b) 30 cm (c) and tilted (d). Photographs are from from underneath the ice shelf, facing out, for (e) barotropic flow and (f) baroclinic flow.

Figure 4: Blocking of depth-independent currents in laboratory. Horizontal velocities from the laboratory experiments are presented for the barotropic flow with the three different ice shelf configurations (Fig. 3b-d). Colors indicate velocity in the y-direction, arrows indicate velocity vectors. (a)-(c) show velocities at the horizontal plane in the center of the current (black lines in (d)-(i)), (d)-(f) show velocities at vertical sections underneath the ice shelf

(green lines in (a)-(c)) and (g)-(i) in front of it (magenta lines in (a)-(c)). Dashed and shadowed rectangles indicate the ice shelf, grey shading indicates topography and grey lines are lines of constant water thickness that the current is expected to follow. White areas are not measured/ missing data. The cyan arrow beneath the scale arrow in (a) - (c) indicate the temporal standard deviation of the velocity and magenta bar indicates the error (Methods).

Methods

Mooring data

Three moorings were deployed on 29 January 2016 and recovered on 18 January 2018 on the western flank of Siple Island (Fig. 1). Two of the moorings were deployed 11-14 km from the ice shelf at depths of 600 m (GW2, 73°47.6' S, 127°36.0'S) and 700 m (GW1, 73° 49.8' S, 127° 47.6'S). The third mooring was located 700-750 m from the ice shelf at a depth of 600 m (GW3, 73° 50.0' S, 127°16.6'S), within a Rossby radius (2 km) of the ice front. The moorings were equipped with sensors for temperature, conductivity and pressure from Seabird Electronics (SBE37, SBE39 and SBE56) and Acoustic Doppler Current Profilers (ADCP, Teledyne RD Instruments, 75 and 150 kHz kHz Sentinel). The initial accuracy of the temperature data were 0.002 °C and the resolution was 0.0001 °C. The ADCP data were quality controlled using standard criteria for filtering out bad data and outliers[36] based on quality controls on individual beams and bins recorded by the instrument each ping (percent good returns below 50%, average echo intensity below 40 (counts) and roll and pitch of instrument exceeding 20° filtered out). The raw data (saved at 15 minute temporal resolution) had standard error 1 -1.5 cm/s and were averaged to hourly means.

Hydrographic measurements extended from the bottom to 357 and 305 m below the surface for GW2 and GW1, respectively, with downward looking ADCPs just above the top sensor, and to 288 m below the surface at GW3, with an upward looking ADCP just below the bottom sensor (Fig. 1). Extended Data Figures 1 - 3 show the North- and Eastward velocities recorded at the three locations, together with temperature. Conservative temperature and absolute salinity in Fig. 1 were calculated following TEOS-10[37]

The along-slope directions were defined as true bearings of 135° for GW1, 110° for GW2, and 70° for GW3, based on the IBCSO[31] database (Fig. 1).

Ice shelf data

The position of the ice front shown in Figure 1 was manually digitized from Sentinel-1 Synthetic Aperture Radar images recorded in January of 2016, 2017 and 2018. Level-1 Ground Range Detected images, projected to ground range using the Earth ellipsoid model WGS84 with pixel size of 40x40 m. Getz ice shelf is characterized by surface structures parallel to the calving front[38]. This is the most common pattern observed among west Antarctic ice shelves and gives the type of calving front studied. The mean ice equivalent thickness of Getz ice shelf is 286 m[3], comparable to the average of ice shelves in the Amundsen Sea (273 m). This indicates that Getz ice shelf is representative for the area.

Baroclinic and barotropic velocity components

According to thermal wind balance[22] the baroclinic velocity component is expected to be largest in the dense layer below the thermocline and small in the well-mixed water above it. Since the present velocity data do not cover the upper water column (Extended Data Fig. 1) the barotropic (U_{BT}) and baroclinic (U_{BC}) velocity components have to be estimated based on the data at hand. Three different methods were employed and compared,

(i) Assuming that the barotropic velocity component is given by the vertical average of the measured water column. While this method would give an accurate estimate in flows that have a comparatively thin baroclinic layer and/or a strong barotropic current, it will likely overestimate the barotropic current in the present data since only the bottom half of the water column is measured.

(ii) Assuming that the barotropic velocity component is given by the vertical average of the velocity from 150 m above the seabed to the upper end of the measured volume. This method will give an accurate estimate when the thermocline is closer than 150 m to the seabed but will otherwise overestimate the barotropic velocity component.

(iii) Assuming that the barotropic velocity component is given by the average velocity in the water above the thermocline. This method gives the most accurate result, but a disadvantage is that the thermocline was not always covered by the mooring data. By choosing the thermocline level to be at -0.5 °C, barotropic velocity estimates were obtained for nearly the complete record (Extended Data Fig. 1, lower panels).

Using any of the above methods, U_{BT} and U_{BC} can be calculated by

$$\begin{aligned} &U_{BC}(z,t) = U(z,t) - U_{BT}(t) \\ &U_{BT}(t) = \frac{1}{(Z_0 - Z_1)} \int_{Z_0}^{Z_1} U(\xi,t)\,d\xi \ , \end{aligned} \qquad (1)$$

where $U(z,t)$ is the velocity measured at the moorings for various depths z and times t, ξ is the integration variable, and the integral limits Z_0 and Z_1 are given by one of the following[27]:

(i) Z_0 = seabed and Z_1 is the upper end of the measured water column.

(ii) Z_0 = 150 m above the seabed and Z_1 is the upper end of the measured water column

(iii) Z_0 is the -0.5 °C isotherm and Z_1 is the upper end of the measured water column

Extended Data Figure 4 shows time series of the three estimates (i) - (iii) of the barotropic velocities over the two years. Extended Data Figure 5 shows the average velocity (thick lines) together with the three alternative barotropic components (thin lines Extended Data Fig. 5A), the baroclinic component (Extended Data Fig. 5B) and the temperature (Extended Data Fig.

5C). In Figure 2 the barotropic velocity component was defined according to (ii) above, i.e. red lines in Extended Data Figure 4 and dashed lines in Extended Data Figure 5A. Similar results were obtained using the other two definitions of Z_0 and Z_1, which is in accordance with [27].

Heat transport calculations

Assuming that the width of the flow is bounded by the sloping topography (as suggested by the laboratory experiments), the heat transport H [J/s] toward the glacier can be estimated by

$$H = W\int_{D}^{\eta} \rho C_P U(T - T_{REF})d\xi, \tag{2}$$

where W [m] is the width of the sloping channel side, D is the bottom elevation, η is the top of the mooring, ρ [kg m^{-3}] is density, C_P [J K^{-1} kg^{-1}] is the specific heat capacity, U [m s^{-1}] is the (average) along-channel velocity, T [K] the temperature and T_{REF} the temperature to which the water cools after interaction with glacial ice. Assuming that all the water cools to freezing temperature, (2) is given by

$$H = W\rho C_P \int_{D}^{\eta} U(T - T_F)dz\,.$$

where T_F [K] is the in situ freezing temperature (which decreases with pressure and salinity). The heat flux induced by the barotropic respectively baroclinic velocity components is then given by $H = H_{BT} + H_{BC}$ where

$$H_{BC} = W\rho C_P \int_{D}^{\eta} U_{BC}(T - T_F)dz \tag{3}$$

$$H_{BT} = W\rho C_P \int_{D}^{\eta} U_{BT}(T - T_F)dz\,, \tag{4}$$

and the barotropic (U_{BT}) and baroclinic (U_{BC}) velocity components are given by (1). In Extended Data Figure 6, time series of H, H_{BT} and H_{BC} were calculated using W = 10 km, C_P = 3.968 kJ kg^{-1} K^{-1}, *in situ* freezing temperature[39], *in situ* density[39], and definition (ii) for the barotropic velocity (1). The temperature- and velocity data were re-gridded to a common grid using daily averages and linear interpolation in the vertical with 8 m cell size.

Extended Data Table 1 shows the temporal average of the heat flux calculated from (2) - (4) and each of the three methods (i) - (iii). As discussed, the barotropic velocity is likely overestimated with method (i) which gives smaller baroclinic heat flux components for all three moorings. The results of method (ii) and (iii) are quite consistent and shows that the baroclinic heat flux is about 30% at GW1 and GW2 while it is between 90% - 97% at GW3, where the average barotropic velocity is nearly zero.

Heat transport errors

The instrument error in the ADCP is maximum 1.5 cm/s and the real error is significantly lower since an average over many pings was used. This error is of the same order of magnitude as the methodological uncertainty, exemplified by the three methods (Extended Data Fig. 5). In the conversion from velocity to heat transport there is an error involved in the assumption that the data at the mooring site is representative for the entire channel (equation (2)). In the absence of continuous, high resolution sampling across the width of the channel, which would enable an exact estimate of this error, an indication of the uncertainties involved can be obtained by the difference between the results of GW1 and GW2 (Table 1), i.e. about 0.5 TW or 18%. There is also an error caused by the fact that the upper part of the water column is not included in the heat flux calculations. Since the temperature above the measured volume is near freezing temperature (Extended Data Fig. 5), however, this error is relatively small.

Another source of error is the assumption that the flow is steady. By separating velocity and temperature into mean and fluctuating components the impact of temporal variability on the average heat transport can be estimated by

$$\overline{H} = W\rho C_P \overline{\int_D^{\eta} (\overline{U} + U')(\overline{T} + T' - T_F)\,d\xi}\,, \tag{5}$$

where temporal mean is denoted by overbar and fluctuating part is denoted by hyphen. Since the temporal average of the fluctuating part is zero, (5) reduces to

$$\overline{H} = W\rho C_P \int_D^{\eta} (\overline{\overline{U}(T - T_F)} + \overline{U'T'})\,d\xi = \overline{\overline{H}} + \tilde{H}\,, \tag{6}$$

where $\overline{\overline{H}}$ is the contribution from the average velocity and temperature, and $\tilde{H}$ is the contribution from the temporal variability about the mean. Extended Data Table 1 shows the two contributions - the heat flux in all three moorings is caused primarily by the mean and the contribution from the fluctuations is between 6% and 20%.

Theory

In geostrophic flow[20] the momentum equations are dominated by the Coriolis- and the pressure gradient terms, i.e.

$$v = \frac{1}{f\rho}\frac{\partial p}{\partial x} \quad (7)$$

$$u = -\frac{1}{f\rho}\frac{\partial p}{\partial y}, \quad (8)$$

where (u, v) are the velocity components in the (x, y) directions, f (s^{-1}) is the Coriolis parameter and p is the hydrostatic pressure. Assuming that the Coriolis parameter is constant and using the Boussinesq approximation[22], it follows from (7) - (8) that geostrophic velocity is non-divergent, i.e.

$$\frac{\partial u}{\partial x} + \frac{\partial v}{\partial y} = 0. \quad (9)$$

For the simplified case of one active layer, i.e. a well-mixed layer extending from the bottom to either the surface or to the interface separating an active dense layer from an inactive lighter water mass above it, vertical integration of the continuity equation gives[20-22] (using (9) and the fact that the velocities are vertically homogeneous)

$$\frac{\partial \eta}{\partial t} + u\frac{\partial \eta}{\partial x} + v\frac{\partial \eta}{\partial y} - u\frac{\partial D}{\partial x} - v\frac{\partial D}{\partial y} = 0, \quad (10)$$

where η is the upper surface (either the water surface or the dense interface) and D is the bottom elevation. Equation (10) can also be expressed in terms of the layer thickness $H(x, y, t) = \eta(x, y, t) - D(x, y)$ according to

$$\frac{\partial H}{\partial t} + u\frac{\partial H}{\partial x} + v\frac{\partial H}{\partial y} = 0. \quad (11)$$

Steady solutions to (11) have streamlines parallel to lines of constant water column thickness (H), irrespective of the bottom elevation $D(x,y)$ and the pressure (as long as the flow is geostrophic). Equation (11) might appear trivial but the combination of geostrophy and solid upper and lower boundaries has important consequences for the currents entering ice shelf cavities in Antarctica. When an ice shelf is protruding from above, the along-trough flow experienced outside the cavity will be deflected to flow along the ice front instead. Barotropic flow towards Antarctica's ice shelves is thus expected to be blocked from reaching the inner parts of the ice shelf cavities (as seen in Fig. 1). Baroclinic flow, on the other hand, is expected to follow the depth contours into the inner ice shelf cavity.

Laboratory experiments

The laboratory experiments were conducted on the 13-m-diameter rotating platform at Laboratoire des Écoulements Géophysiques et Industriels (LEGI) in Grenoble, France.

A v-shaped channel of size 5 m × 1 m × 0.5 m and a 2% slope (Extended Data Fig. 7) was built at the center of the turntable (red dot Extended Data Fig. 7). Focusing on the dynamics of the flow and ignoring thermodynamic changes such as melting and freezing of ice, a cuboid Plexiglas ice shelf with adjustable elevation and tilt was placed at the lower (closed) end of the channel. The tank was filled with 90 cm of fresh water and rotated clockwise (Southern Hemisphere) with a rotation period of 30 s, giving a Coriolis parameter $f = 0.42\ s^{-1}$.

A source, placed in the center of the left-hand flank of the channel (looking towards the ice shelf) and resting on the topography, pumped water at 60 l/min into the channel. The source was 0.15 m high, 0.25 m wide, 0.25 m long and sloped at the bottom to fit the topography (Extended Data Fig. 7). The outflow area was 0.47 m^2 and had a honeycomb of small tubes to produce a homogeneous laminar flow. For the barotropic experiments the source water was fresh like the ambient water and for the baroclinic experiments it was saline and 2 kg m^{-3} denser than the ambient water. A drainage and skimmer kept the water level constant.

Neutrally buoyant particles (60 μm Dantec Dynamics particles) in the source water were illuminated by a horizontal laser plane (Extended Data Fig. 8) in order to visualize the flow. Two cameras with pixel resolution 2560 × 2160 pixels were mounted above the channel. The footprint of both cameras (Exended Data Fig. 7) gave a resolution of 0.6 mm/pixel. The laser shifted through depth levels starting near the bottom of the channel. For the barotropic experiments 12 different depth levels were used with a vertical distance of dz = 6.2 cm. In order to resolve better the faster-moving dense current and focus on the lower part of the channel, 7 different depth levels with dz = 5.8 cm were used in the baroclinic experiments. At each level, 30 (barotropic experiments) or 20 (baroclinic experiments) consecutive images were taken by both cameras with 0.1 s interval giving a total of 60 s for a complete cycle through all depth levels. The obtained images were used for Particle Image Velocimetry (PIV) calculations with the UVMAT software developed at LEGI (for details see http://servforge.legi.grenoble-inp.fr/projects/soft-uvmat). Independent results were also obtained with a second software, MatPIV (https://www.mn.uio.no/math/english/people/aca/jks/matpiv), and found to agree with UVMAT. Using the pixel per image value, i.e. 0.6 mm/0.5 s for barotropic (every 5 images were used) and 0.6 mm/0.1 s for baroclinic experiments, the velocity error was 1.2 mm/ for the barotropic and 6 mm/s for the baroclinic experiments. The obtained 25 (or 19 for baroclinic experiments) velocity fields for each level were then averaged, which lowered the error further. Figure 4 shows the average of 4-5 cycles at one level, starting at the time when the leading edge reached the ice front, together with the temporal standard deviation of the velocity for that level (cyan arrows) and the error (magenta bars). Outliers (defined as velocities for which the standard deviation exceeds 10 times the average standard deviation) were identified and filtered out. The vertical sections (Fig. 4d-f) were created from the parts of the horizontal slices that occupied +/- 2 cm around the green and magenta lines in Fig. 4.

In addition to the top-view cameras, a side-view camera was mounted outside a glass wall at the side of the tank and GoPro cameras were lowered into the water to get side-view images (Fig. 3 and Extended Data Fig. 8). In the side view images, fluorescent dye (rhodamin) was used for visualization.

The topography was built to mimic a submarine trough topography with depth variations of same magnitude as the ice shelf draft, in similarity with the observations. Geostrophic balance was ensured by choosing flow- and rotation rates so that both the Ekman number Ek (i.e. the frictional force compared to the Coriolis force[20]) and the Rossby number[20] (i.e. the inertial forces compared to the Coriolis force) were smaller than one. The values of the various scales and the non-dimensional numbers are shown in Extended Data Table 1. While the Ekman number was clearly negligible (0.002-0.004), the Rossby number was 0.14-0.2 meaning that ageostrophic effects may amend the process, particularly in regions where the velocity might be larger.

Before each experiment the platform was spun up for 2-3 hours to reach solid body rotation, which was determined by observing the movement of particles. Each experiment was started by opening the source. After about 5 - 10 minutes (faster for baroclinic flow) a current moving towards the ice shelf developed over the sloping part of the topography (Extended Data Fig. 8). Behind the leading edge of the current a semi-steady flow with regions of slower and faster flow moving in the direction of the ice shelf developed (Extended Data Fig. 8d). After interaction with the ice-shelf (15-30 min after experiment start) a counter-current on the opposite side developed, after which the experiment ended.

The baroclinic flow developed faster, was more steady, and was not influenced by the presence of the ice shelf. Instead of returning on the opposite side, the baroclinic flow slowly filled the ice shelf cavity with dense water (Extended Data Fig. 8). More details from the experiments, including detailed drawings, diary, etc is provided at http://servforge.legi.grenoble-inp.fr/projects/pj-coriolis-17iceshelf

Methods references

36. Taylor, J. A. & Jonas, A. M. Maximising Data Return: Towards a quality control strategy for Managing and Processing TRDI ADCP Data Sets from Moored Instrumentation. in *2008 IEEE/OES 9th Working Conference on Current Measurement Technology* 80–88 (IEEE, 2008). doi:10.1109/CCM.2008.4480848

37. IOC, SCOR & IAPSO. *The International thermodynamic equation of seawater, 2010: calculation and use of thermodynamic properties*. *IOC: Manuals and guides (UNESCO Digital Library)* (2010).

38. Wesche, C., Jansen, D. & Dierking, W. Calving Fronts of Antarctica: Mapping and Classification. *Remote Sens.* **5**, 6305–6322 (2013).

39. Fofonoff, N. P. & Millard, R. C. *Algorithms for Computation of Fundamental Properties of Seawater*. *UNESCO Technical Papers in Marine Science* (1983).

40. Darelius, E., Fer. I., Assmann, K. M. & Kim, T. W. Physical oceanography from Mooring UiB1 and UiB4 in the Amundsen Sea. (2018). doi:10.21335/NMDC-1721053841

Data and code availability:

The mooring data analysed during the current study (raw data for Figure 1-2 and extended data Figures 1-6) are available at the Norwegian Marine Data Centre (https://doi.org/10.21335/NMDC-1721053841[40], GW1-2) and at SOOS data base at NODC (https://doi.org/10.25921/n07g-f935 and https://doi.org/10.25921/6pwp-1791, GW3)

Raw data obtained from the PIV calculations (raw data for Figure 4 and Extended Data Figure 9) are available at Zenodo (https://zenodo.org/record/3543624).

The PIV calculations were conducted with the matlab software UVMAT developed at LEGI available at http://servforge.legi.grenoble-inp.fr/projects/soft-uvmat. Independent results were also obtained with the MatPIV package available at https://www.mn.uio.no/math/english/people/aca/jks/matpiv.

Extended data legends

Extended Data Figure 1: Two year time series of velocity and temperature from GW1 mooring. Time series of (a) eastward velocity, (b) northward velocity and (c) temperature for the GW1 mooring. Black lines in (c) indicate positions of Microcats (thick lines) and SBE56 (thin lines).

Extended Data Figure 2: Two year time series of velocity and temperature from GW2 mooring. Time series of (a) eastward velocity, (b) northward velocity and (c) temperature for the GW2 mooring. Black lines in (c) indicate positions of Microcats (thick lines) and SBE56 (thin lines).

Extended Data Figure 3: Two year time series of velocity and temperature from GW3 mooring. Time series of (a) eastward velocity, (b) northward velocity and (c) temperature for the GW3 mooring. Black lines in (c) indicate positions of Microcats (thick lines) and SBE56 (thin lines).

Extended Data Figure 4: Comparison of methods for calculating barotropic component. Along-slope barotropic current component based on option (i): vertical average, option (ii): vertical average of the water more than 150 m above seabed, and option (iii): vertical average of water above the -0.5° isotherm according to legend. (a) Mooring GW1, 3-day averaged (b) Mooring GW2, 3-day averaged (c) Mooring GW3, 3-day averaged.

Extended Data Figure 5: The barotropic velocity is larger for GW1 and GW2 than GW3, the baroclinic velocity and the temperature increase towards the bottom. (a) Thick lines show average along-slope velocities as a function of distance above bottom, with colors indicating mooring (legend). Thin vertical lines show the barotropic components estimated according to method (i) (dotted lines), method (ii) (dashed lines), and method (iii) (solid lines). (b) Baroclinic velocity components as a function of distance above bottom. (c) Average temperature as a function of distance above bottom.

Extended Data Figure 6: The barotropic heat flux component is larger than the baroclinic for GW1 and GW2. Time series of total heat flux and the barotropic and baroclinic components using expression (2) and definition (ii) of barotropic velocity. (a) Mooring GW1 (b) Mooring GW2 (c) Mooring GW3.

Extended Data Figure 7. Experiment set-up and dimensions. (a) Top view drawing of v-shaped channel (blue), ice shelf (white), camera views (PCO1, green, PCO2, orange) and the source (to scale). (b) Side view drawing looking into the ice shelf facing South (c) Side view drawing looking East (d)-(f) Top views of topography (gray scale, color bar) and water column thickness (colored lines, labels) for (d) Ice shelf draft 0 cm (e) Ice shelf draft 30 cm, tilted (f) ice shelf draft 30 cm, horizontal.

Extended Data Figure 8: Photographs from the experiments. (a) Top view showing the experimental set-up with the horizontal and vertical laser sheets. (b) Technicians and students preparing for an experiment (c) Time series showing the ice shelf cavity filling up with dense water for the baroclinic experiments (d) Top view photograph showing a barotropic current moving towards the ice shelf.

Extended Data Figure 9. No blocking of depth-varying currents in laboratory. Horizontal velocities from the laboratory experiments are presented for the baroclinic flow with the three different ice shelf configurations (Fig. 3b-d). Colors indicate velocity in the y-direction, arrows indicate velocity vectors. (a)-(c) show velocities at the horizontal plane in the center of the current (black lines in (d)-(i)), (d)-(f) show velocities at vertical sections underneath the ice shelf (green lines in (a)-(c)) and (g)-(i) in front of it (magenta lines in (a)-(c)). Dashed and shadowed rectangles indicate the ice shelf, grey shading indicates topography and grey lines are bathymetric lines that the current is expected to follow. White areas are not measured/ missing data. The cyan arrow beneath the scale arrow in (a) - (c) indicate the temporal standard deviation of the velocity and magenta bar indicates the error (Methods).

Extended Data Table 1: Part of heat flux caused by the barotropic current component is large compared to that caused by the baroclinic component. Average heat flux (H) and its barotropic (eq. (3)) and baroclinic (eq. (4)) components using different definitions of barotropic velocity (i) Vertical average over the entire measured water column (ii) Vertical average over the measured water column more than 150 m above the bottom (iii) Vertical average over the measured water column above the -0.5° isotherm (see Methods). Also shown is the part of the heat flux induced by the average velocity and temperature ($\overline{\mathbf{H}}$) and their fluctuating components ($\tilde{\mathbf{H}}$) according to equation (6).

Extended Data Table 2: Non-dimensional scales are similar in laboratory experiment and observations. Scale values for velocity (*U*), density difference ($\Delta\rho$), Coriolis parameter (*f*), depth (*H*), width (*L*), molecular (in laboratory) or turbulent (in field) viscosity (*v*) and the derived Ekman depth (δ_E), Ekman number (*Ek*), Rossby radius (L_R) and Rossby number (*Ro*). Observational parameters for velocity and density difference were obtained from the GW1 and GW2 mooirng data, while the bathymetric parameters were obtained from [31]. The viscosity scale is a bulk eddy viscosity[22].

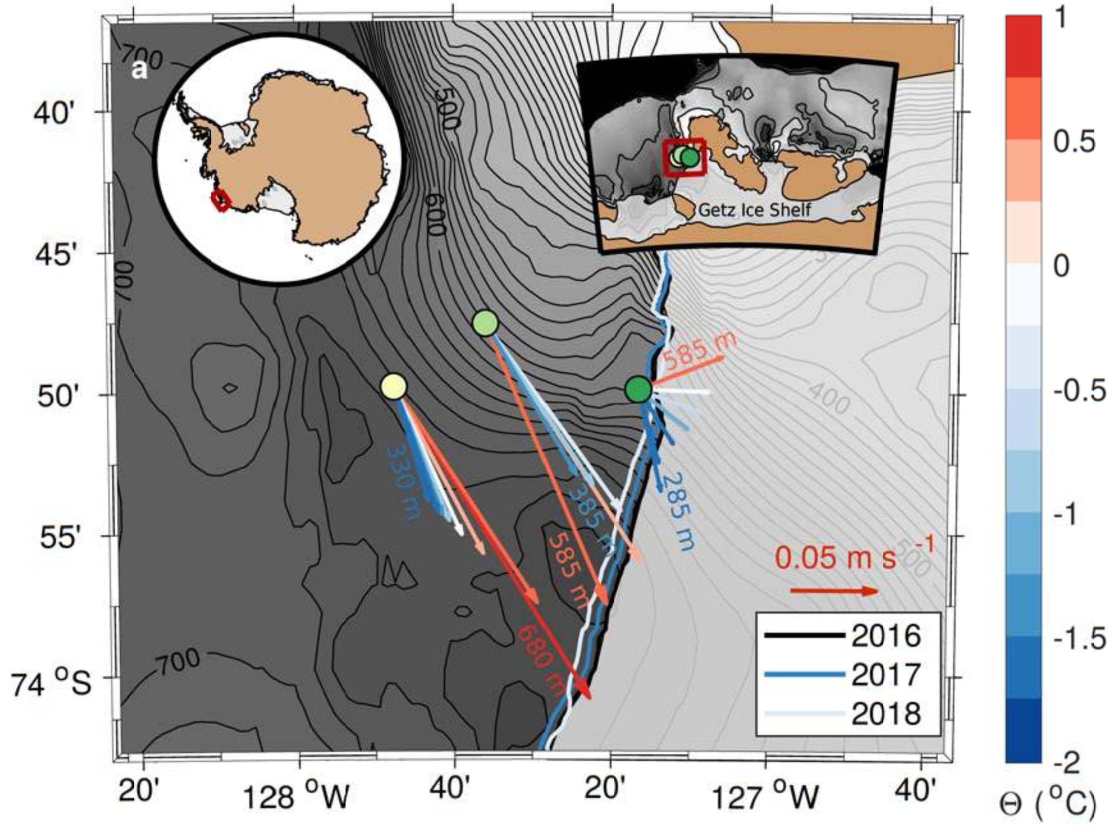
a
Getz Ice Shelf
700
500
600
400
500
330 m
385 m
585 m
285 m
585 m
680 m
0.05 m s-1
2016
2017
2018
40'
45'
50'
55'
74 °S
20'
128 °W
40'
20'
127 °W
40'
1
0.5
0
-0.5
-1
-1.5
-2
Θ (°C)

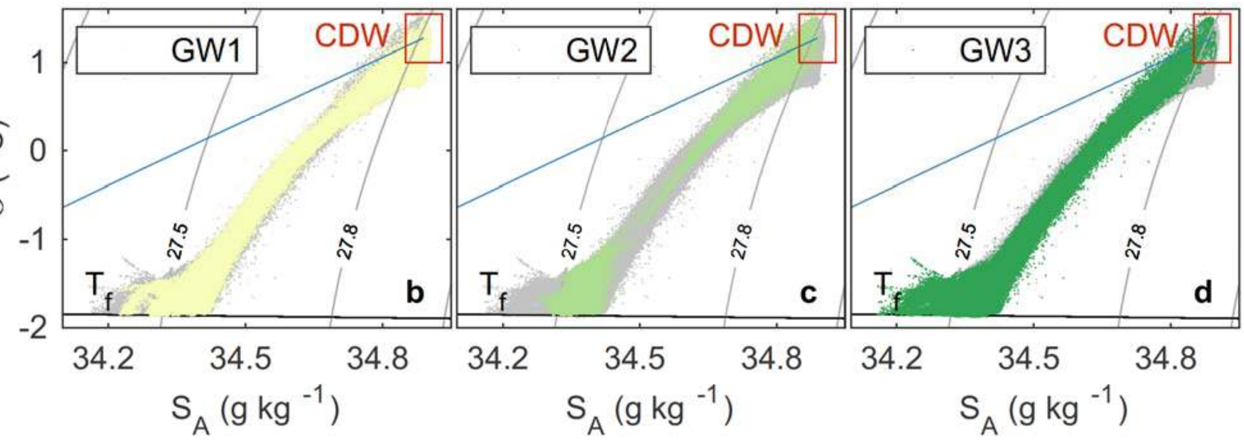

GW1
GW2
GW3
CDW
CDW
CDW
Θ (°C)
1
0
-1
-2
27.5
27.8
T_f
b
c
d
34.2
34.5
34.8
S_A (g kg -1)

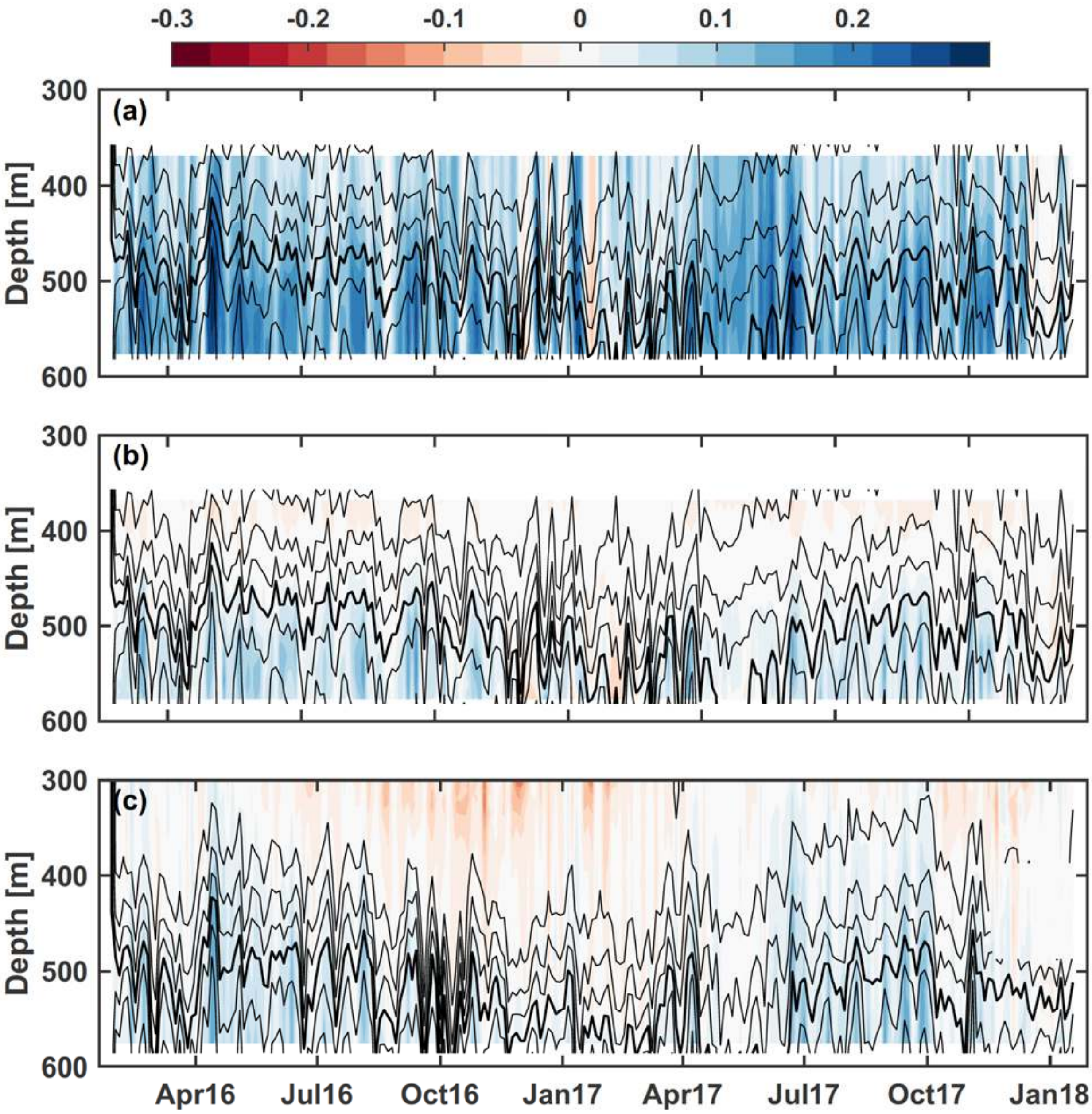

-0.3
-0.2
-0.1
0
0.1
0.2
(a)
(b)
(c)
Depth [m]
300
400
500
600
Apr16
Jul16
Oct16
Jan17
Apr17
Jul17
Oct17
Jan18

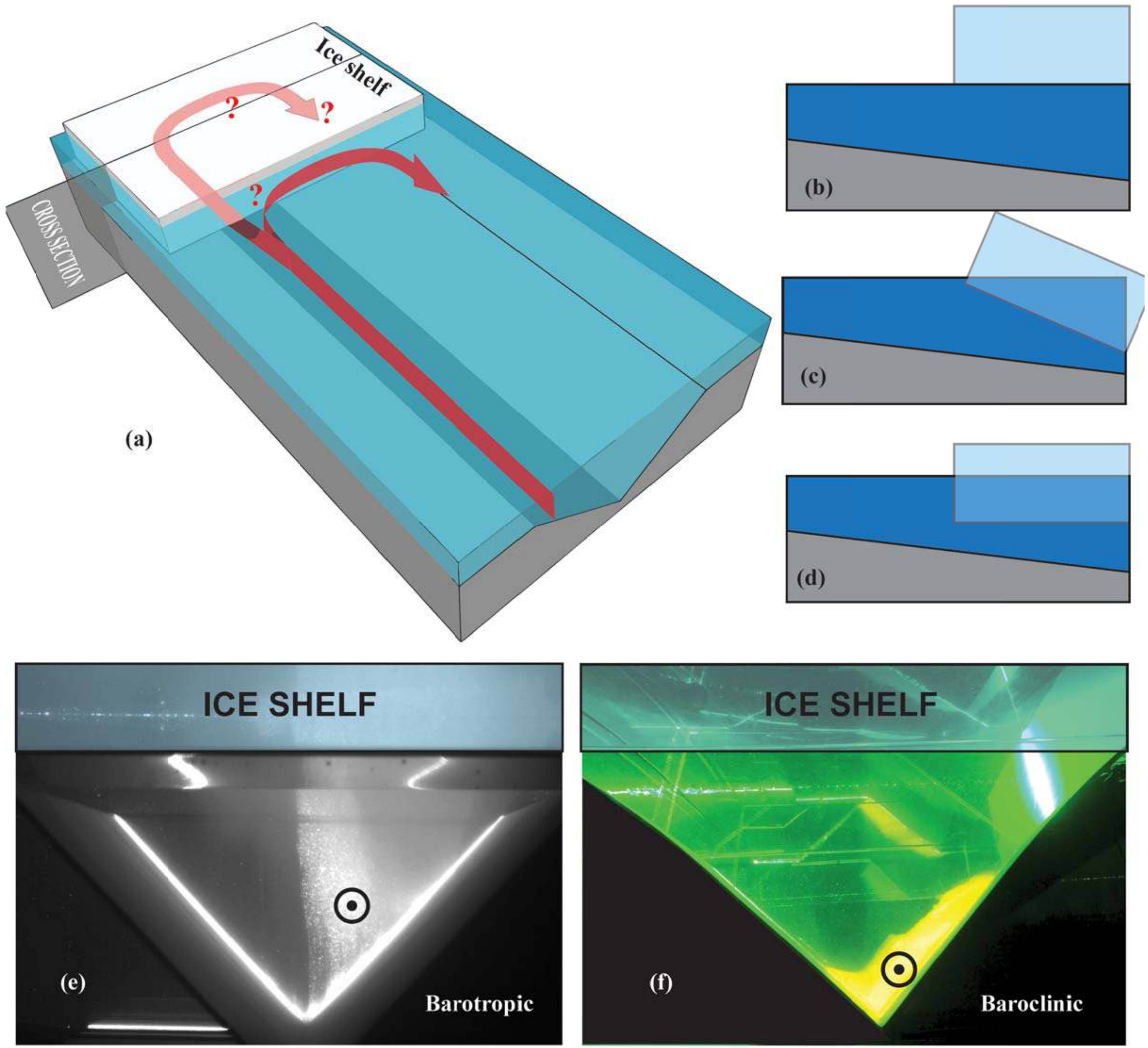
Ice shelf
?
?
?
CROSS SECTION
(a)
(b)
(c)
(d)
ICE SHELF
(e)
Barotropic
ICE SHELF
(f)
Baroclinic

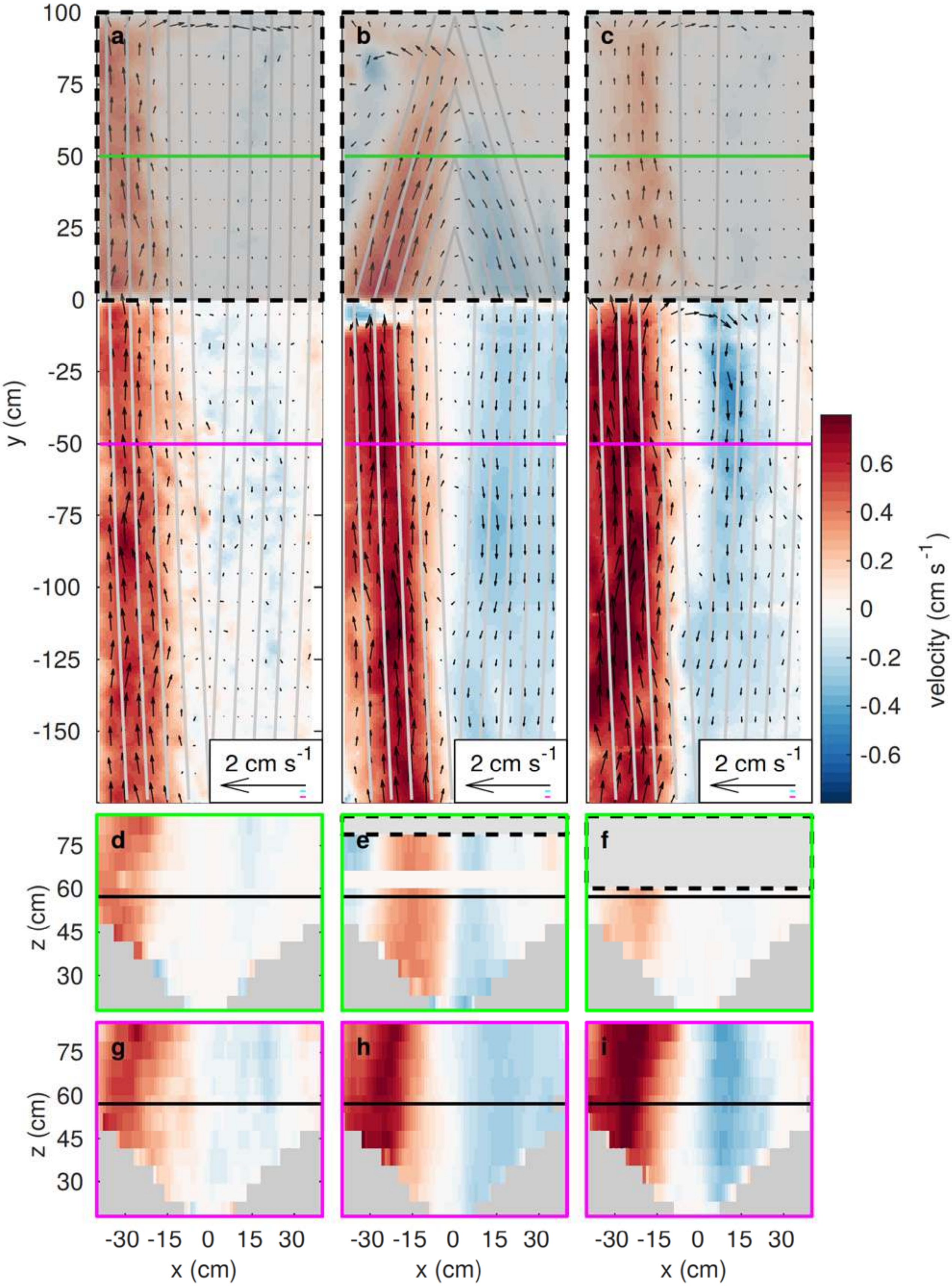

a
b
c
d
e
f
g
h
i
y (cm)
z (cm)
x (cm)
2 cm s-1
velocity (cm s-1)
100
75
50
25
0
-25
-50
-75
-100
-125
-150
0.6
0.4
0.2
0
-0.2
-0.4
-0.6
-30 -15 0 15 30

Extended data

Extended Data Figure 1: Two year time series of velocity and temperature from GW1 mooring. Time series of (a) eastward velocity, (b) northward velocity and (c) temperature for the GW1 mooring. Black lines in (c) indicate positions of Microcats (thick lines) and SBE56 (thin lines).

Extended Data Figure 2: Two year time series of velocity and temperature from GW2 mooring. Time series of (a) eastward velocity, (b) northward velocity and (c) temperature for the GW2 mooring. Black lines in (c) indicate positions of Microcats (thick lines) and SBE56 (thin lines).

Extended Data Figure 3: Two year time series of velocity and temperature from GW3 mooring. Time series of (a) eastward velocity, (b) northward velocity and (c) temperature for the GW3 mooring. Black lines in (c) indicate positions of Microcats (thick lines) and SBE56 (thin lines).

Extended Data Figure 4: Comparison of methods for calculating barotropic component. Along-slope barotropic current component based on option (i): vertical average, option (ii): vertical average of the water more than 150 m above seabed, and option (iii): vertical average of water above the -0.5^{o} isotherm according to legend. (a) Mooring GW1, 3-day averaged (b) Mooring GW2, 3-day averaged (c) Mooring GW3, 3-day averaged.

Extended Data Figure 5: The barotropic velocity is larger for GW1 and GW2 than GW3, the baroclinic velocity and the temperature increase towards the bottom. (a) Thick lines show average along-slope velocities as a function of distance above bottom, with colors indicating mooring (legend). Thin vertical lines show the barotropic components estimated according to method (i) (dotted lines), method (ii) (dashed lines), and method (iii) (solid lines). (b) Baroclinic velocity components as a function of distance above bottom. (c) Average temperature as a function of distance above bottom.

Extended Data Figure 6: The barotropic heat flux component is larger than the baroclinic for GW1 and GW2. Time series of total heat flux and the barotropic and baroclinic components using expression (2) and definition (ii) of barotropic velocity. (a) Mooring GW1 (b) Mooring GW2 (c) Mooring GW3.

Extended Data Figure 7. Experiment set-up and dimensions. (a) Top view drawing of v-shaped channel (blue), ice shelf (white), camera views (PCO1, green, PCO2, orange) and the source (to scale). (b) Side view drawing looking into the ice shelf facing South (c) Side view drawing looking East (d)-(f) Top views of topography (gray scale, color bar) and water column thickness (colored lines, labels) for (d) Ice shelf draft 0 cm (e) Ice shelf draft 30 cm, tilted (f) ice shelf draft 30 cm, horizontal.

Extended Data Figure 8: Photographs from the experiments. (a) Top view showing the experimental set-up with the horizontal and vertical laser sheets. (b) Technicians and students preparing for an experiment (c) Time series showing the ice shelf cavity filling up with dense water for the baroclinic experiments (d) Top view photograph showing a barotropic current moving towards the ice shelf.

Extended Data Figure 9. No blocking of depth-varying currents in laboratory. Horizontal velocities from the laboratory experiments are presented for the baroclinic flow with the three different ice shelf configurations (Fig. 3b-d). Colors indicate velocity in the y-direction, arrows indicate velocity vectors. (a)-(c) show velocities at the horizontal plane in the center of the current (black lines in (d)-(i)), (d)-(f) show velocities at vertical sections underneath the ice shelf (green lines in (a)-(c)) and (g)-(i) in front of it (magenta lines in (a)-(c)). Dashed and shadowed rectangles indicate the ice shelf, grey shading indicates topography and grey lines are bathymetric lines that the current is expected to follow. White areas are not measured/ missing data. The cyan arrow beneath the scale arrow in (a) - (c) indicate the temporal standard deviation of the velocity and magenta bar indicates the error (Methods).

Extended Data Table 1: Part of heat flux caused by the barotropic current component is large compared to that caused by the baroclinic component. Average heat flux (H) and its barotropic (eq. (3)) and baroclinic (eq. (4)) components using different definitions of barotropic velocity (i) Vertical average over the entire measured water column (ii) Vertical average over the measured water column more than 150 m above the bottom (iii) Vertical average over the measured water column above the -0.5° isotherm (see Methods). Also shown is the part of the heat flux induced by the average velocity and temperature ($\overline{\mathbf{H}}$) and their fluctuating components ($\tilde{\mathbf{H}}$) according to equation (6).

Extended Data Table 2: Non-dimensional scales are similar in laboratory experiment and observations. Scale values for velocity (*U*), density difference ($\Delta\rho$), Coriolis parameter (*f*), depth (*H*), width *(L)*, molecular (in laboratory) or turbulent (in field) viscosity (ν) and the derived Ekman depth (δ_E), Ekman number (*Ek*), Rossby radius (L_R) and Rossby number (*Ro*). Observational parameters for velocity and density difference were obtained from the GW1 and GW2 mooirng data, while the bathymetric parameters were obtained from [31]. The viscosity scale is a bulk eddy viscosity[22].

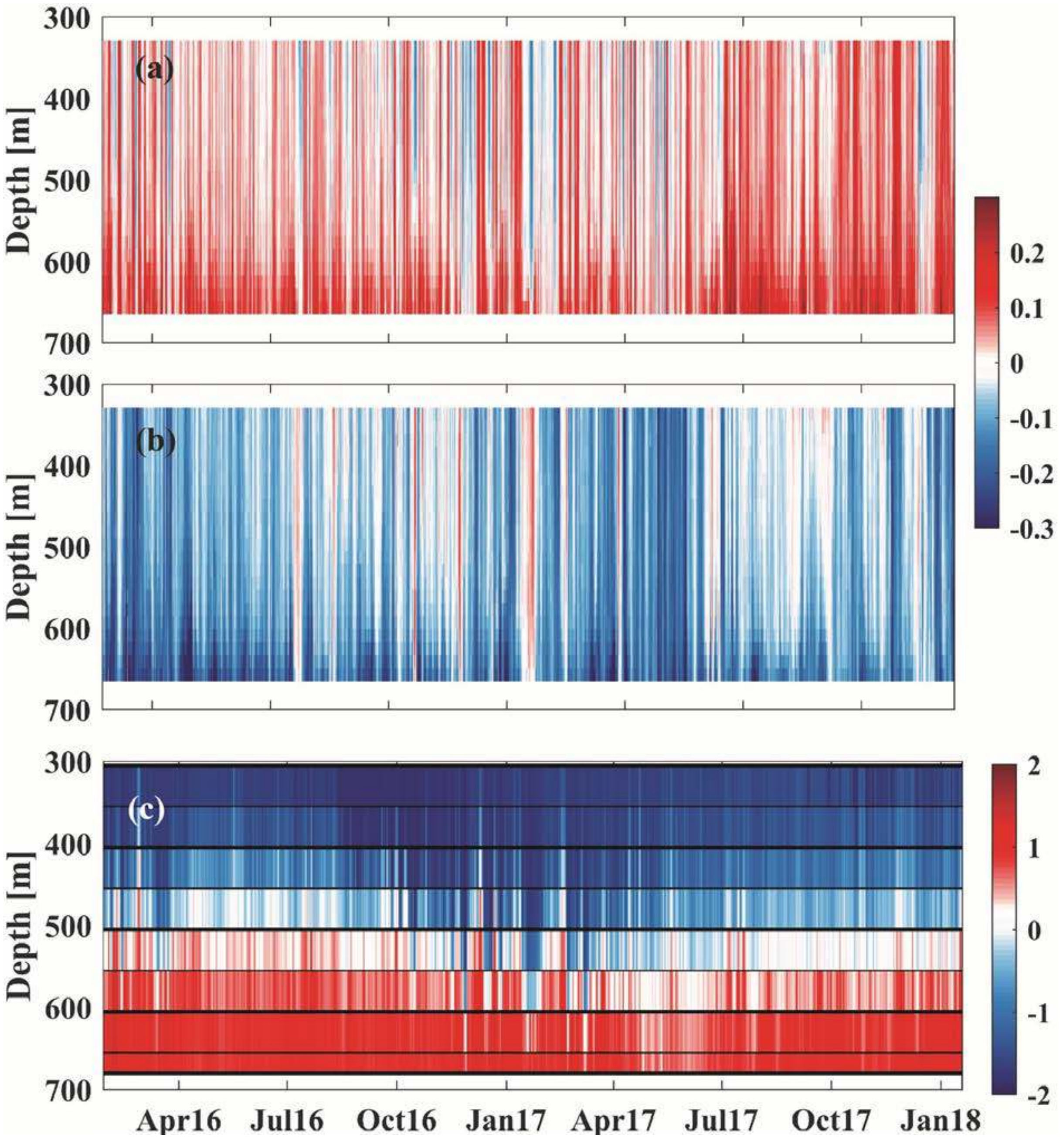

(a)
(b)
(c)
Depth [m]
300
400
500
600
700
0.2
0.1
0
-0.1
-0.2
-0.3
2
1
0
-1
-2
Apr16
Jul16
Oct16
Jan17
Apr17
Jul17
Oct17
Jan18

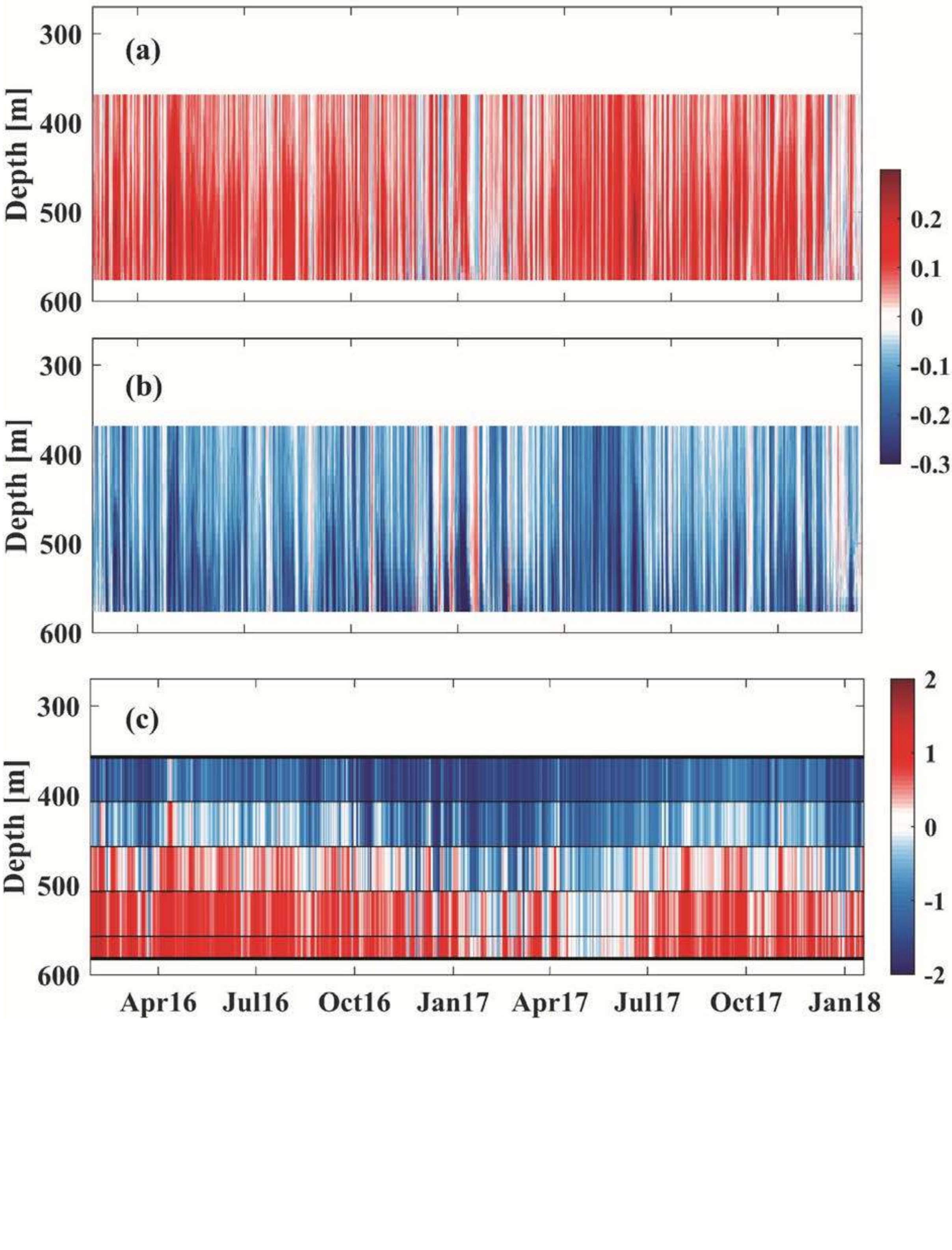

(a)
(b)
(c)
Depth [m]
300
400
500
600
0.2
0.1
0
-0.1
-0.2
-0.3
2
1
0
-1
-2
Apr16
Jul16
Oct16
Jan17
Apr17
Jul17
Oct17
Jan18

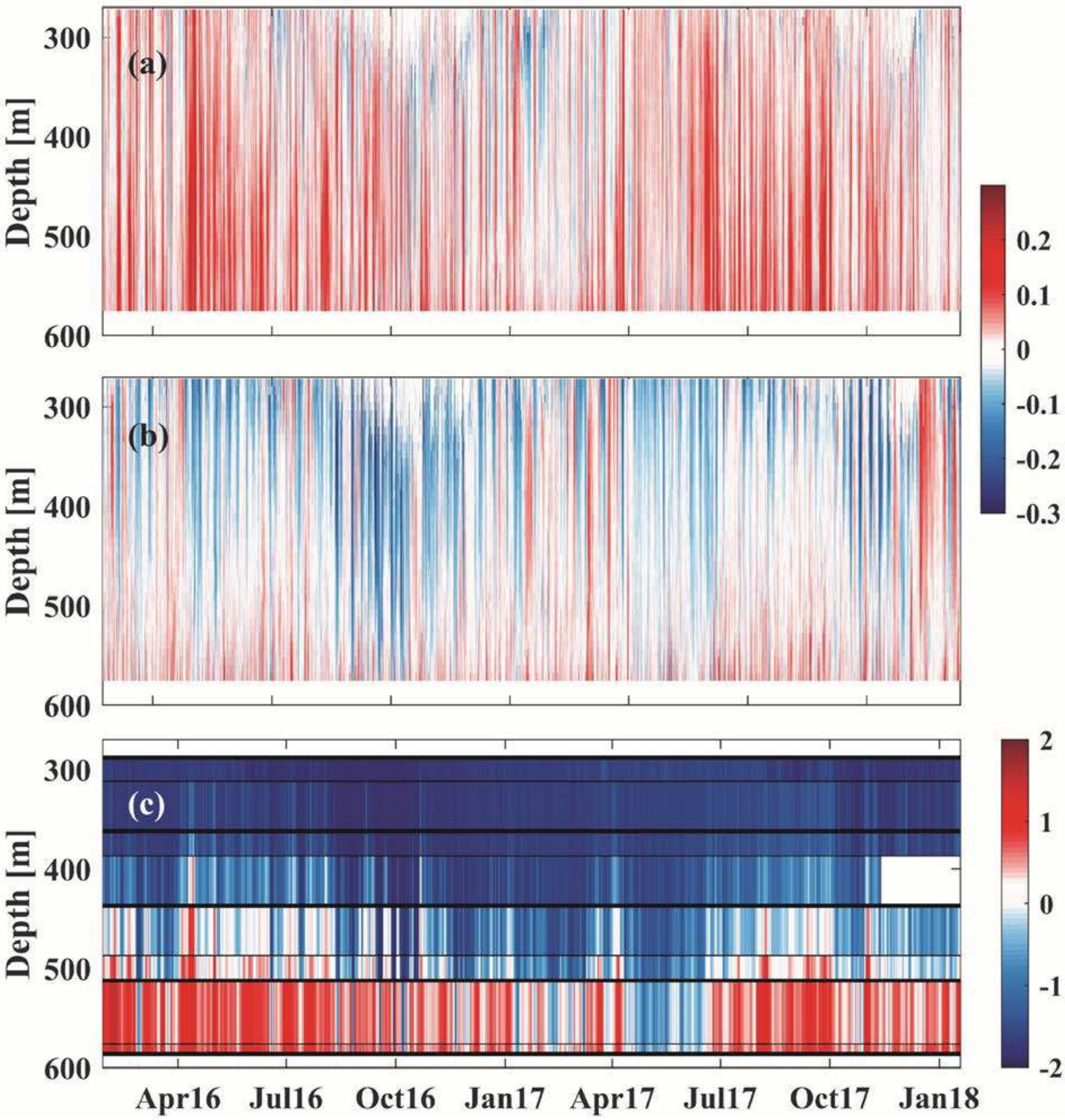

(a)
(b)
(c)
Depth [m]
300
400
500
600
0.2
0.1
0
-0.1
-0.2
-0.3
2
1
0
-1
-2
Apr16
Jul16
Oct16
Jan17
Apr17
Jul17
Oct17
Jan18

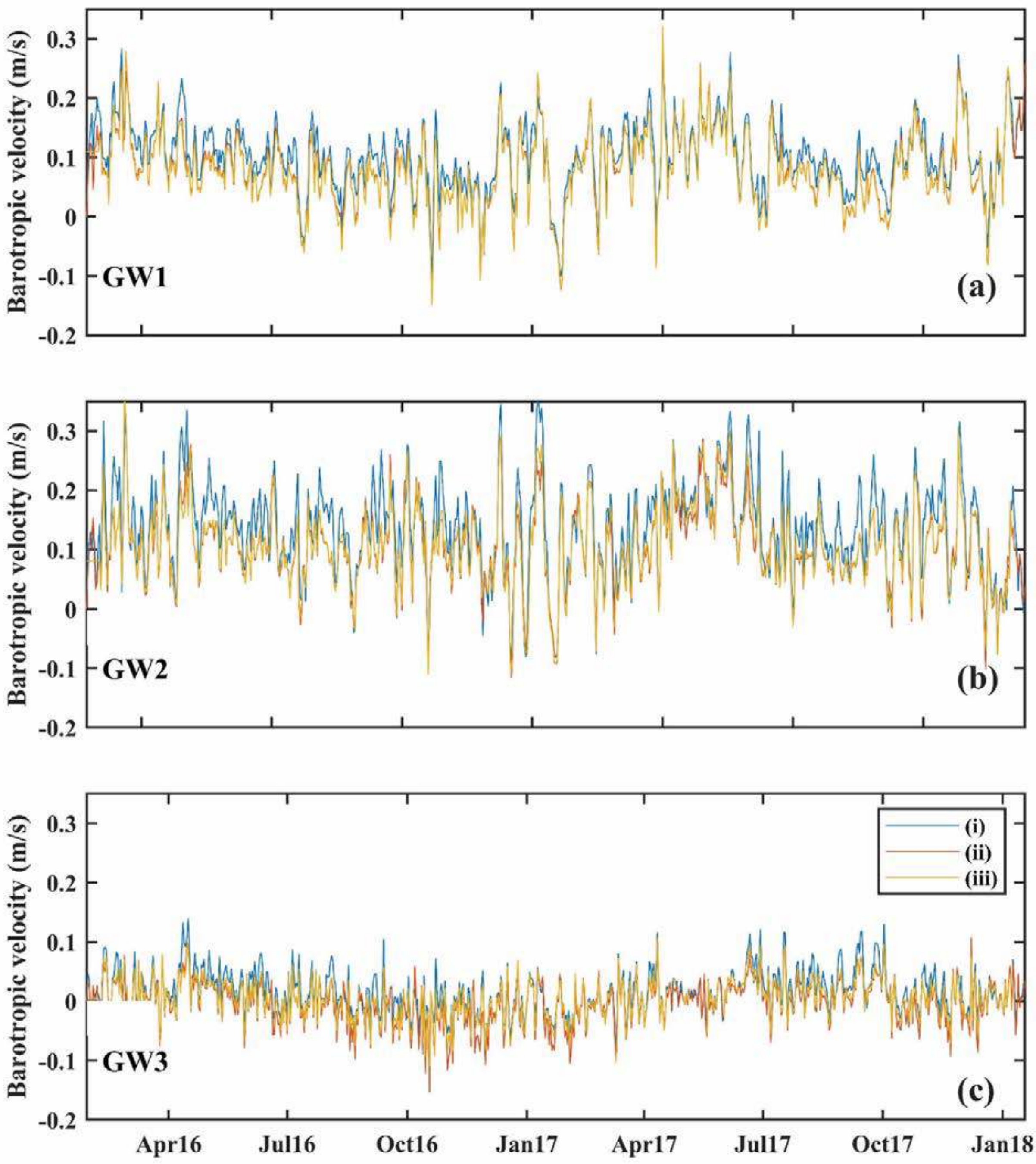

Barotropic velocity (m/s)
0.3
0.2
0.1
0
-0.1
-0.2
GW1
(a)
GW2
(b)
GW3
(c)
(i)
(ii)
(iii)
Apr16
Jul16
Oct16
Jan17
Apr17
Jul17
Oct17
Jan18

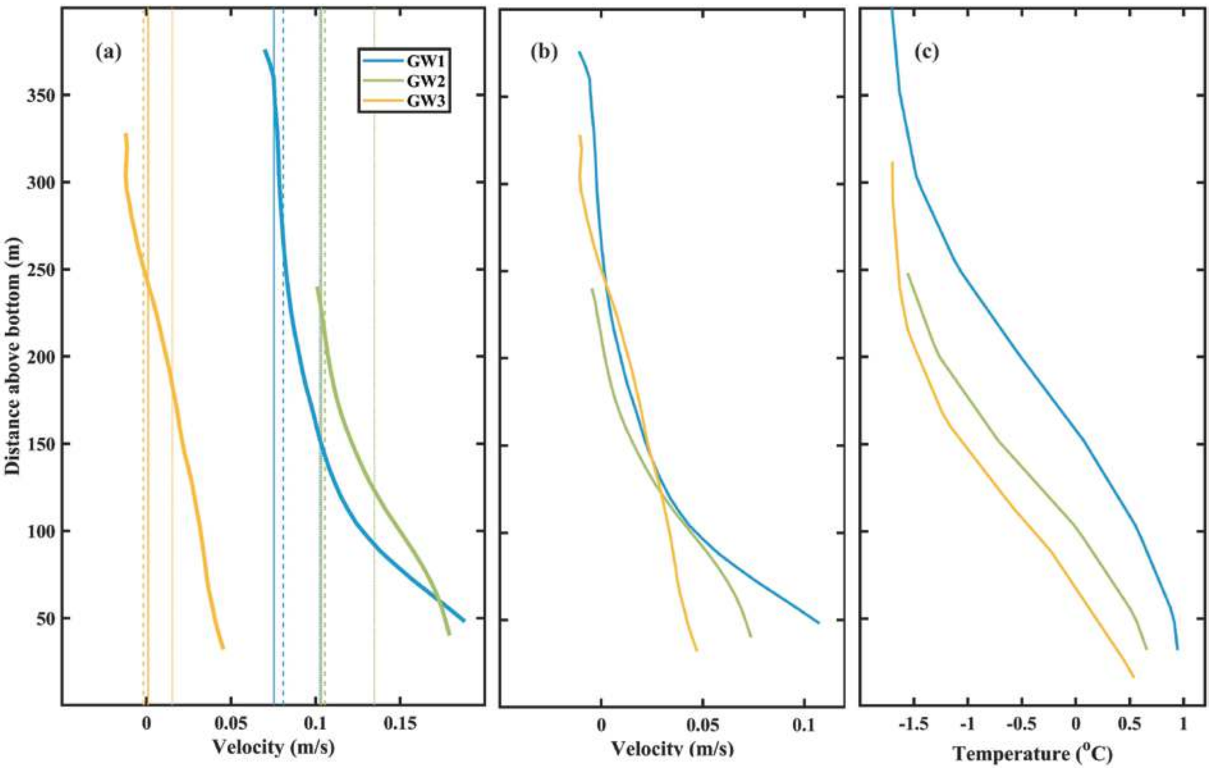

(a)
GW1
GW2
GW3
Distance above bottom (m)
350
300
250
200
150
100
50
0
0.05
0.1
0.15
Velocity (m/s)
(b)
0
0.05
0.1
Velocity (m/s)
(c)
-1.5
-1
-0.5
0
0.5
1
Temperature (°C)

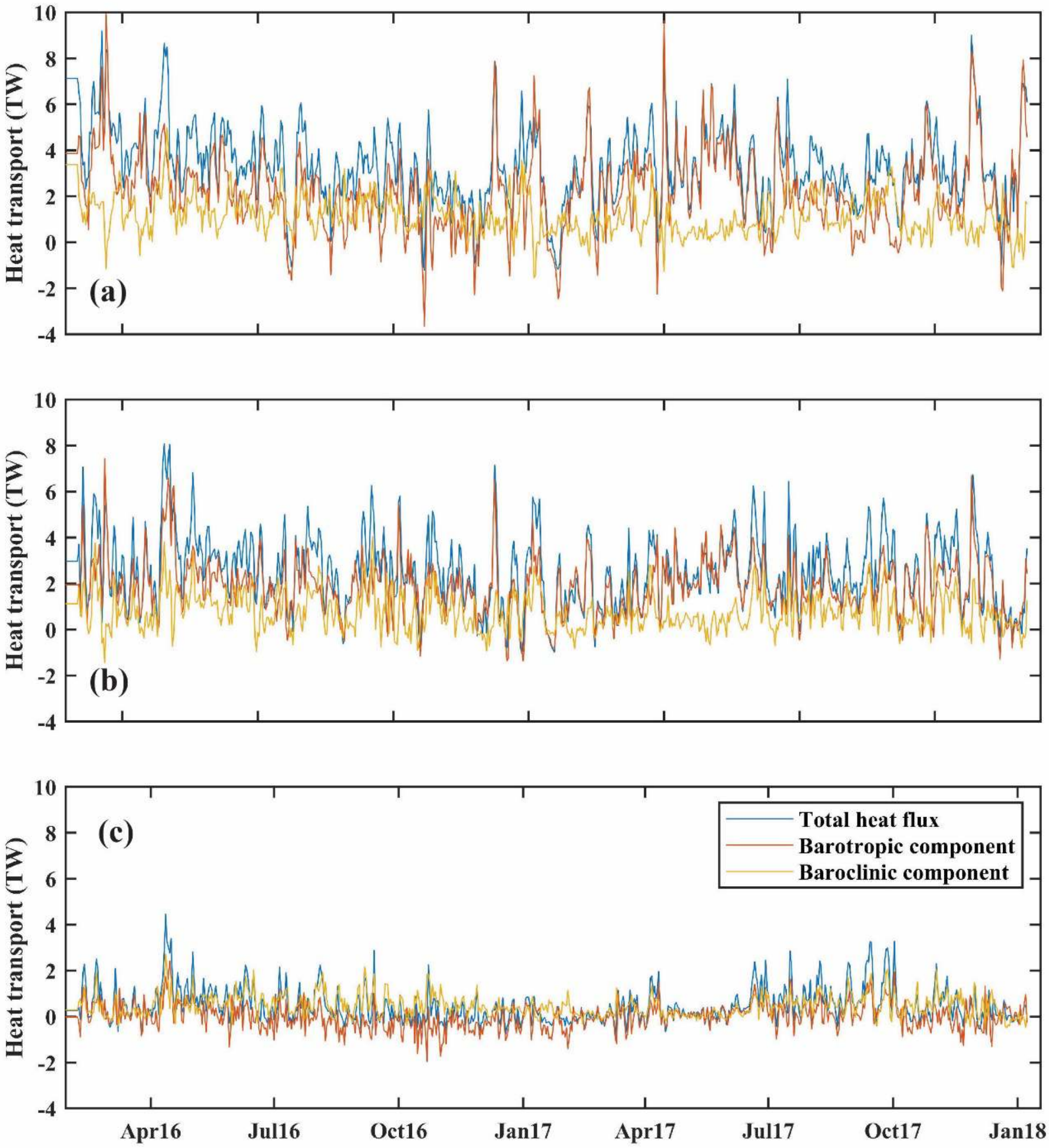
Heat transport (TW)
(a)
(b)
(c)
Total heat flux
Barotropic component
Baroclinic component
Apr16
Jul16
Oct16
Jan17
Apr17
Jul17
Oct17
Jan18
10
8
6
4
2
0
-2
-4

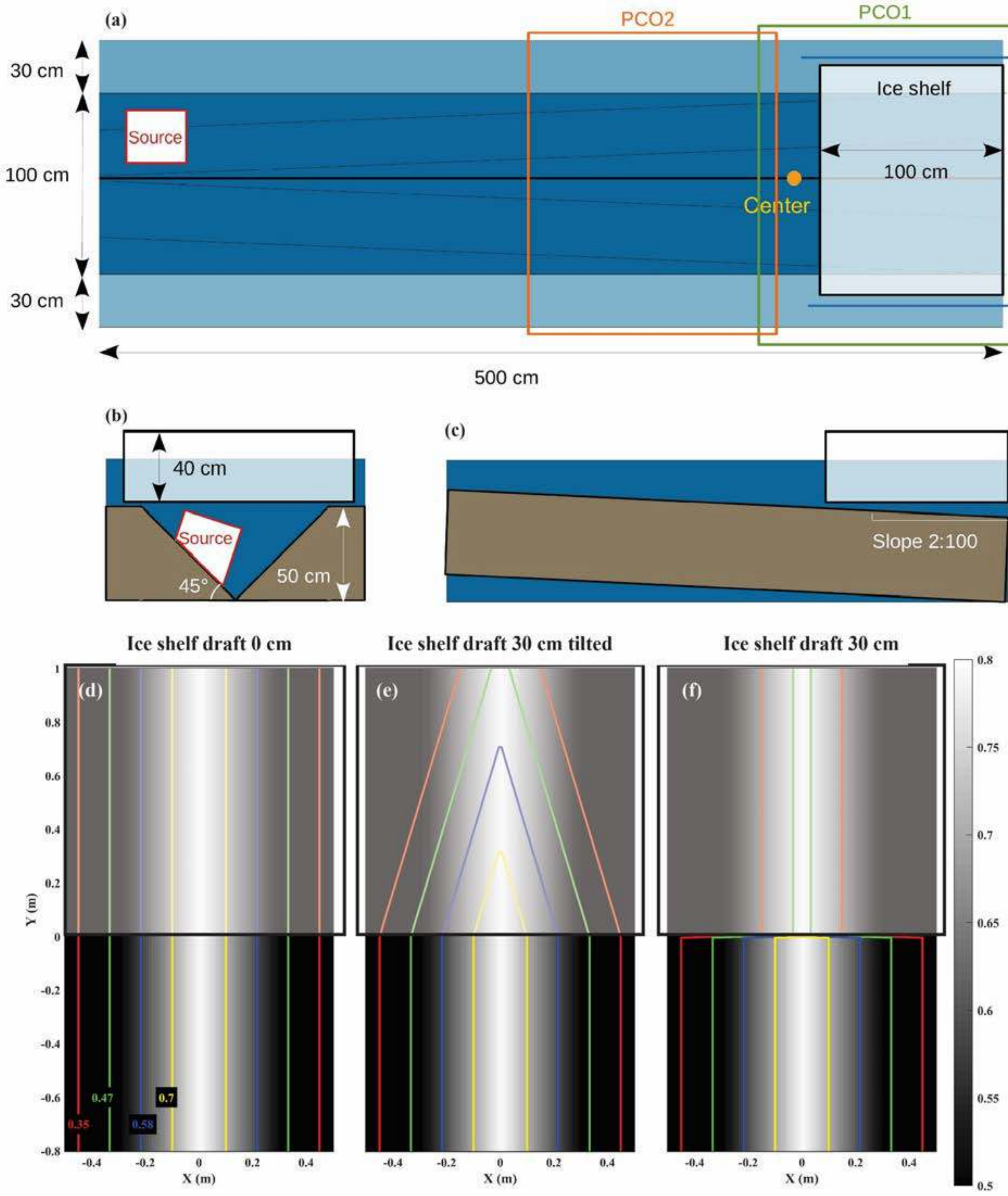

(a)
PCO2
PCO1
30 cm
100 cm
30 cm
Source
Ice shelf
100 cm
Center
500 cm
(b)
40 cm
Source
45°
50 cm
(c)
Slope 2:100
Ice shelf draft 0 cm
Ice shelf draft 30 cm tilted
Ice shelf draft 30 cm
(d)
(e)
(f)
Y (m)
X (m)
0.35
0.47
0.58
0.7

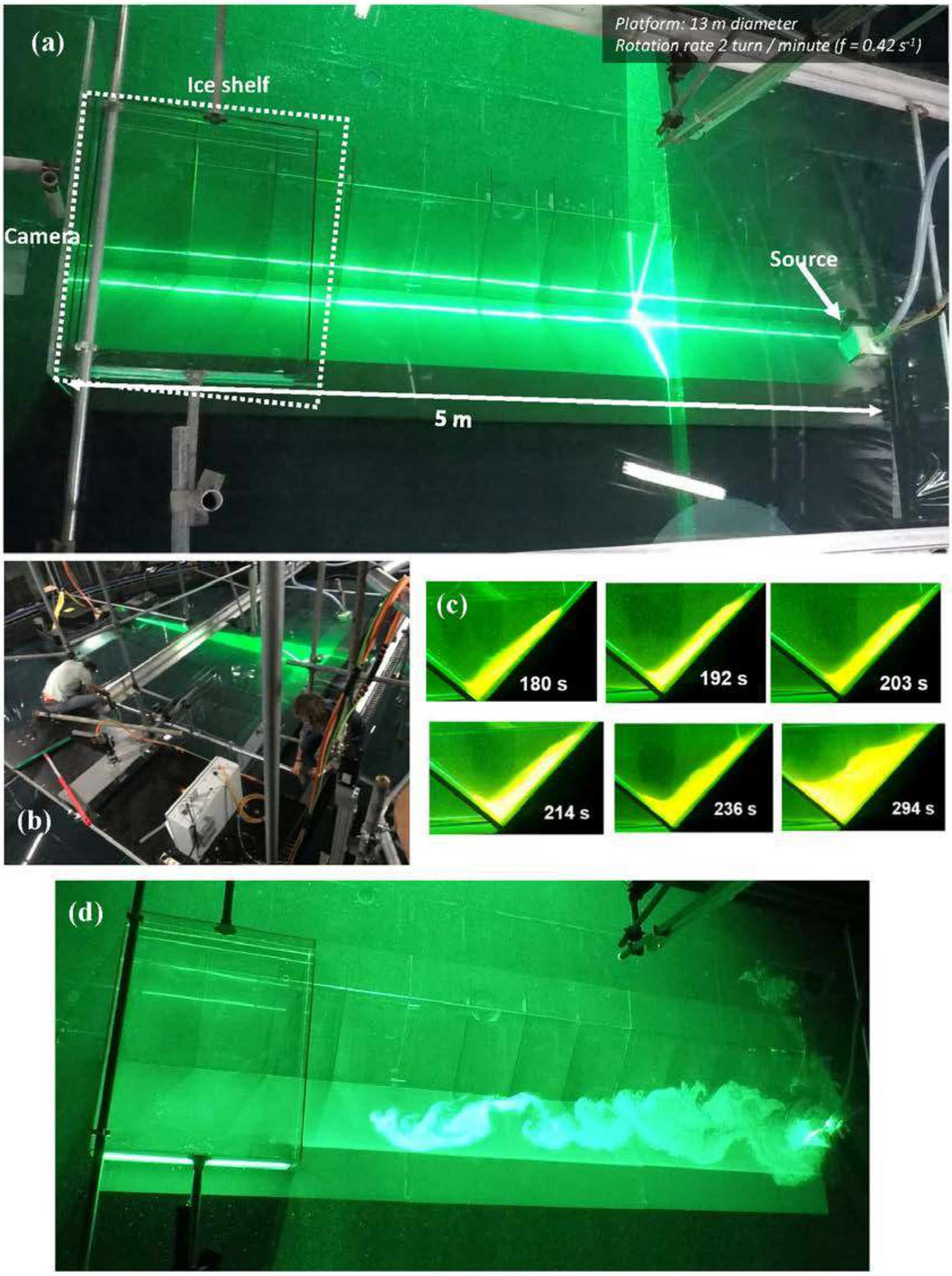
(a)
Platform: 13 m diameter
Rotation rate 2 turn / minute (f = 0.42 s⁻¹)
Ice shelf
Camera
Source
5 m
(b)
(c)
180 s
192 s
203 s
214 s
236 s
294 s
(d)

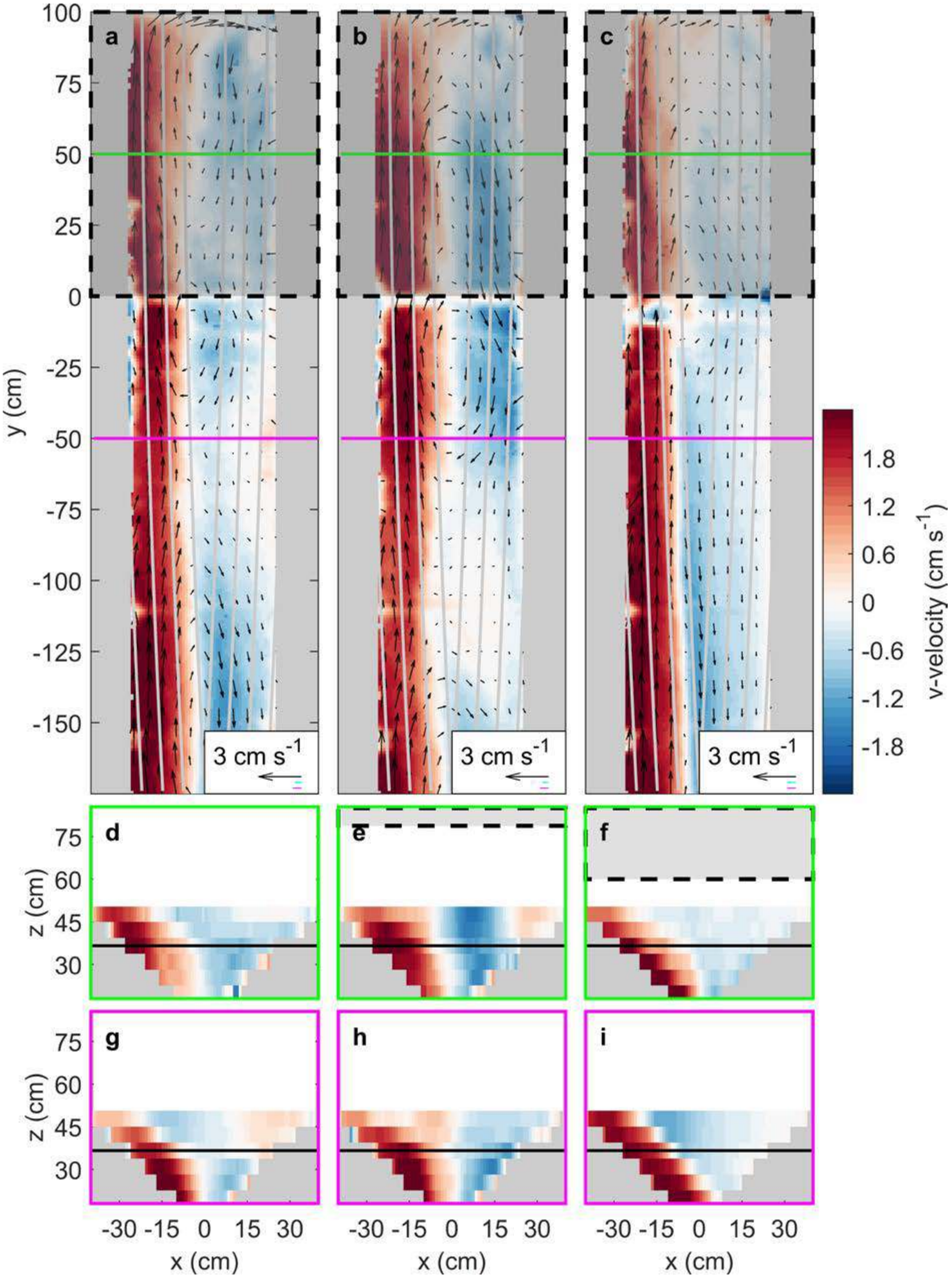

a
b
c
d
e
f
g
h
i
y (cm)
z (cm)
x (cm)
3 cm s-1
v-velocity (cm s-1)
100
75
50
25
0
-25
-50
-75
-100
-125
-150
1.8
1.2
0.6
0
-0.6
-1.2
-1.8
75
60
45
30
-30 -15 0 15 30

Extended Data Table 1: Part of heat flux caused by the barotropic current component is large compared to that caused by the baroclinic component.

	GW1	GW2	GW3
H	2.8 TW	2.27 TW	0.47 TW
$\overline{\mathbf{H}}$	2.64 TW (94%)	2.14 TW (94%)	0.38 TW (80%)
$\tilde{\mathbf{H}}$	0.16 TW (6%)	0.13 TW (6%)	0.09 TW (20%)
$\mathbf{H}_{BT}$ **(method (i))**	2.49 TW (89%)	2.11 TW (93%)	0.28 TW (60%)
$\mathbf{H}_{BC}$ **(method (i))**	0.31 TW (11%)	0.16 TW (7%)	0.19 TW (40%)
$\mathbf{H}_{BT}$ **(method (ii))**	1.96 TW (70%)	1.61 TW (71%)	0.01 TW (3%)
$\mathbf{H}_{BC}$ **(method (ii))**	0.84 TW (30%)	0.66 TW (29%)	0.46 TW (97%)
$\mathbf{H}_{BT}$ **(method (iii))**	1.88 TW (67%)	1.59 TW (70%)	0.05 TW (10%)
$\mathbf{H}_{BC}$ **(method (iii))**	0.92 TW (33%)	0.68 TW (30%)	0.42 TW (90%)

Extended Data Table 2: Non-dimensional scales are similar in laboratory experiment and observations.

Symbol [unit]	Laboratory	Obervations	Description
U [m s^{-1}]	0.03	0.2	Velocity
$\Delta\rho$ [kg m^{-3}]	2	0.3	Density difference
f [s^{-1}]	0.42	10^{-4}	Coriolis parameter
H [m]	0.5	500	Depth
L [m]	0.5	10^{4}	Width
ν [m^2 s^{-1}]	10^{-6}	10^{-4}	Viscosity
$\delta_E = \sqrt{\nu/f}$ **[m]**	0.0015	1	Ekman depth
$Ek = \delta_E^2/H^2$	$0.9\cdot10^{-5}$	$0.4\cdot10^{-5}$	Ekman number
$L_R = U/f$ **[m]**	0.07	2000	Rossby radius
$Ro = L_R/L$	0.14	0.2	Rossby number